CELLULAR NEUROSCIENCE

Sequential compound fusion and kiss-and-run mediate exo- and endocytosis in excitable cells

Lihao Ge[1]†, Wonchul Shin[1]†, Gianvito Arpino[1]†, Lisi Wei[1], Chung Yu Chan[1], Christopher K. E. Bleck[2], Weidong Zhao[1]‡, Ling-Gang Wu[1]*

Vesicle fusion at preestablished plasma membrane release sites releases transmitters and hormones to mediate fundamental functions like neuronal network activities and fight-or-flight responses. This half-a-century-old concept—fusion at well-established release sites in excitable cells—needs to be modified to include the sequential compound fusion reported here—vesicle fusion at previously fused Ω-shaped vesicular membrane. With superresolution STED microscopy in excitable neuroendocrine chromaffin cells, we real-time visualized sequential compound fusion pore openings and content releases in generating multivesicular and asynchronous release from single release sites, which enhances exocytosis strength and dynamic ranges in excitable cells. We also visualized subsequent compound fusion pore closure, a new mode of endocytosis termed compound kiss-and-run that enhances vesicle recycling capacity. These results suggest modifying current exo-endocytosis concepts by including rapid release-site assembly at fused vesicle membrane, where sequential compound fusion and kiss-and-run take place to enhance exo-endocytosis capacity and dynamic ranges.

INTRODUCTION

Vesicle fusion releases transmitters, hormones, and peptides to mediate many physiological functions, such as synaptic transmission, fight or flight response, and controlling blood glucose level, which is relevant to diabetes (*1*–*4*). In excitable cells, including neurons and endocrine cells, physiological stimulations often come as brief depolarizations repeated at various frequencies for various periods of time, which evoke repeated release of transmitters and hormones to meet various physiological functions (*2*, *3*). To sustain such repeated release, vesicle must move from the cytosol to the plasma membrane and dock at the release sites (*2*, *3*, *5*). Upon calcium influx induced by depolarization, docked vesicles open a fusion pore to release vesicular contents (*2*, *6*, *7*). Most releases are synchronized after a brief depolarization (*8*). This synchronized release may faithfully translate a brief presynaptic firing into brief postsynaptic activity for synaptic transmission at synapses (*3*, *8*). Often, a small fraction of vesicle fusion is not synchronized but asynchronized, producing releases at various times after the brief depolarization (*3*, *8*). Asynchronized release may translate a brief depolarization to a more prolonged vesicular content release that may be needed physiologically for some neurons and endocrine cells (*8*).

At a single release site, a single vesicle is often released (called monovesicular release) in response to a brief depolarization, such as an action potential at nerve terminals. However, multivesicular release, either synchronized or desynchronized after a brief depolarization, may also take place at single release sites to enhance the capacity of vesicular content release, which may increase synaptic strength at synapses and exocytosis capacity in endocrine cells (*1*, *9*–*12*).

After a vesicle opens a fusion pore to release vesicular contents, the vesicle may (i) close its fusion pore, called kiss-and-run, to recycle fused vesicles economically and rapidly, or (ii) merge with the plasma membrane via fusion pore dilation (called full-collapse fusion) or shrinking of the fusing vesicle (called shrink-fusion) (*13*–*25*). Vesicle merging at the plasma membrane and subsequent clearance of the merged vesicular membrane and proteins from the release site may allow for another vesicle to dock at the just emptied docking site, fusion of which may thus allow for sustaining release during repeated stimulations (*2*, *5*, *13*, *24*, *26*, *27*). Vesicle merging at the plasma membrane also necessitates classical endocytosis that transforms merged flat vesicular membrane into vesicles (*13*, *24*, *28*), which, together with kiss-and-run, recycles fusing vesicles and sustains release during repeated stimulation in secretory cells (*17*, *21*, *25*).

Our understanding of fundamental fusion steps and modes in neurons and endocrine cells discussed above, including vesicle docking, mono- or multivesicular release at single release sites, synchronized or asynchronized release, kiss-and-run, or classical endocytosis for vesicle recycling, is constructed under the assumption that vesicles fuse at the well-established release sites at the plasma membrane (*1*, *2*). Despite being generally accepted, this assumption has not been tested in live cells. Against this assumption, sequential compound fusion—vesicle fusion at the top or side of a previously fused vesicular Ω-shaped structure that forms an 8-shaped membrane structure—was proposed two decades ago in nonexcitable cells containing extremely large (~1 to 5 μm) granules that release contents extremely slowly (~10 s to minutes) (*29*–*31*). If this form of fusion occurs in excitable neurons and endocrine cells, current models of exocytosis and endocytosis may have to be changed accordingly to accommodate this new mechanism. For example, sequential compound fusion may save the final movement of vesicles to the original release site by allowing for vesicle docking at the just-fused, Ω-shaped vesicular membrane structure. Unlike the traditional view that release sites are well-established structures, rapid establishment of release sites at the top or side of the just fused vesicular Ω-shaped membrane must take place to enable sequential compound fusion. Sequential compound fusion may contribute to mediating multivesicular

[1]National Institute of Neurological Disorders and Stroke, 35 Convent Dr., Bldg. 35, Rm. 2B-1012, Bethesda, MD 20892, USA. [2]National Heart, Lung, and Blood Institute, Bethesda, MD 20892, USA.
*Corresponding author. Email: wul@ninds.nih.gov
†These authors contributed equally to this work.
‡Present address: Department of Developmental Cell Biology, China Medical University, Shenyang, China.

release at single release sites and asynchronized release that may enhance the strength of exocytosis (*1*). If sequential compound fusion is followed by fusion pore closure, a new form of kiss-and-run may contribute to recycling of fused vesicles crucial for sustaining exocytosis in secretory cells. Despite these possibilities that may conceptually change our view on fundamental release steps and exo- and endocytosis modes, the concept of sequential compound fusion remains to be established. This is because its dynamics of vesicular membrane structural changes, fusion pore, and vesicular content release have not been directly observed either in nonexcitable cells where the concept was proposed or in excitable cells. Sequential compound fusion has therefore been generally neglected in current fusion and endocytosis models for excitable neurons and endocrine cells (*1*, *6*–*8*).

In the present work, we tested the fundamental assumption—depolarization induces fusion at well-established release sites—by performing superresolution stimulated emission depletion (STED) imaging of membrane dynamics, fusion pore dynamics, and vesicular content release dynamics simultaneously in ~1500 live neuroendocrine chromaffin cells (*23*, *24*). We visualized the membrane dynamics, fusion pore dynamics, and content release dynamics of sequential compound fusion in live cells, providing the direct evidence missing in decades of studies to fully establish the concept of sequential compound fusion. Furthermore, we found a new form of endocytosis following sequential compound fusion, the pore closure after sequential compound fusion pore opening, termed here as compound kiss-and-run. We showed that sequential compound fusion and compound kiss-and-run contribute to vesicle docking/priming, multivesicular release, asynchronized release, and endocytosis, all of which are crucial in determining the strength and dynamic range of exocytosis (*1*, *8*, *9*, *32*). These results suggest modifying current models of exo- and endocytosis by including sequential compound fusion and compound kiss-and-run as new modes of exo-endocytosis.

RESULTS

Observing sequential compound fusion and fusion on preformed Ω-profile in real time

To visualize membrane and pore dynamics of fusion, we transfected enhanced green fluorescent protein (EGFP) or mNeonGreen attached to phospholipase C delta PH domain (PH_G), which binds to Phosphatidylinositol 4,5-bisphosphate [$PI(4,5)P_2$] at, and thus labels the plasma membrane in neuroendocrine cells, the primary cultured bovine adrenal chromaffin cell (Fig. 1A) (*22*, *23*). We added Atto 532 (A532) in the bath, which enters and thus labels fusing vesicles' Ω-shaped profiles (Fig. 1A) (*21*, *23*). To evoke exocytosis, we performed voltage-clamp recording at chromaffin cells and delivered

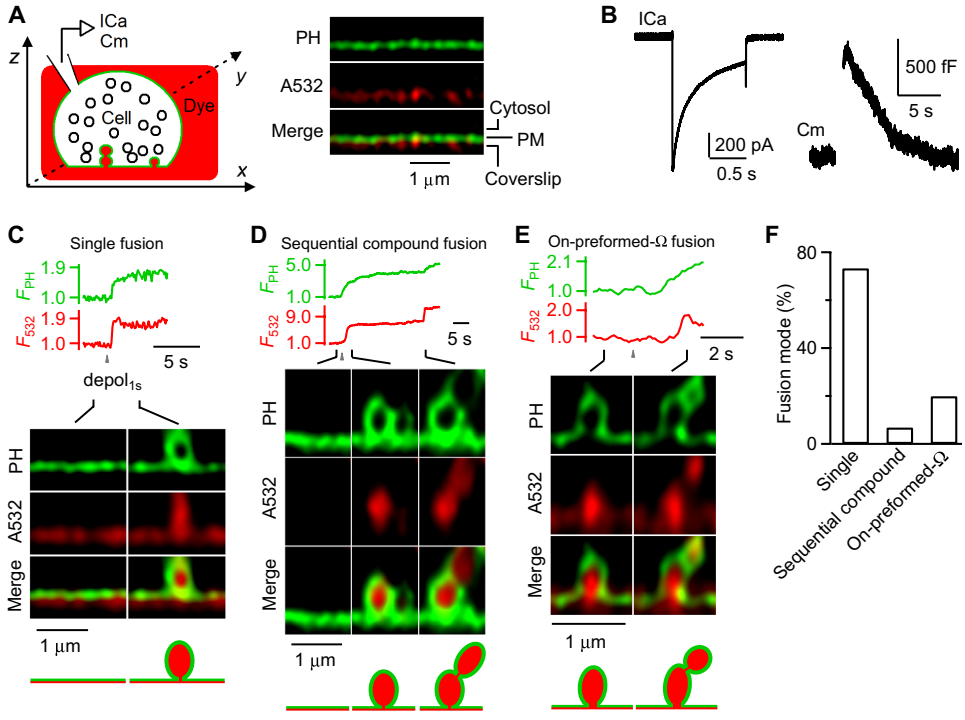

Fig. 1. Real-time visualization of sequential compound fusion and fusion on preformed Ω-profiles in live cells. (**A**) Left: Setup drawing. The cell's membrane is labeled with PH_G (green), and bath was labeled with A532 (red). ICa and Cm (capacitance) are recorded from the whole-cell pipette. Right: XZ plane images of the PH_G-labeled plasma membrane (green) and A532-labeled bath solution (red) between the plasma membrane (PM) and the coverslip in a fraction of a cell (near cell bottom) in resting conditions. Cytosol, PM, and coverslip locations are labeled. (**B**) Sampled ICa and Cm change induced by $depol_{1s}$ from a chromaffin cell—$depol_{1s}$ induced a large calcium current, a large capacitance jump reflecting exocytosis, and the capacitance decay following the jump reflecting endocytosis. (**C** to **E**) Ω_{PH} fluorescence (F_{PH}, normalized to baseline), A532 spot fluorescence (F_{532}, normalized to baseline), and STED XZ plane images at times indicated with lines showing single vesicle fusion (C), sequential compound fusion (D), and on-preformed-Ω fusion (E) induced by $depol_{1s}$ (gray triangle). F_{PH} and F_{532} were collected from fusing vesicle(s). (**F**) The percentage of single vesicle fusion, sequential compound fusion, and on-preformed-Ω fusion observed with STED imaging of PH_G and A532 at the XZ plane (336 events from 274 cells showing these fusion events).

a 1-s depolarization (−80 to +10 mV) via a pipette at the whole-cell configuration, which induced calcium currents (Fig. 1B), capacitance changes reflecting exo- and endocytosis (Fig. 1B), and fusion events observed with STED microscopy of PH_G and A532 (Fig. 1, C to E).

STED images of PH_G and A532 were acquired at the XZ plane (across the cell-bottom membrane) every 26 to 300 ms per frame for ~1 to 2 min, while the Y location was fixed at about the cell center (Fig. 1A; applies to all STED imaging in this study). Each cell was subjected to only one $depol_{1s}$ to avoid whole-cell exo- and endocytosis run-down (*21*, *23*). Image data were collected from a large number of cells, 1211 cells, at the voltage-clamp configuration.

A total of 336 PH_G-labeled Ω-shaped profiles filled with A532 (Ω_{PH}) appeared within a single image frame (26 to 300 ms), reflecting vesicle fusion that allowed for PH_G and A532 diffusion from the plasma membrane and the bath solution to the fusion-generated Ω-profile (Fig. 1, C to F). Among 336 Ω_{PH}, 247 Ω_{PH} (73.5%) appeared at the flat plasma membrane (Fig. 1, C and F, and movie S1), reflecting single vesicle fusion [for details, see (*22*, *23*, *24*)]; 23 Ω_{PH} (6.9%) appeared at the flat plasma membrane but followed at 0.2 to 85 s later on Ω_{PH}'s top or side by a sudden appearance of another Ω_{PH}, forming an 8-shaped structure reflecting sequential compound fusion (Fig. 1, D and F, and movie S2); 66 Ω_{PH} (19.6%) appeared on the top or side of Ω_{PH} preformed before $depol_{1s}$ (termed on-preformed-Ω fusion), which also formed an 8-shaped structure (Fig. 1, E and F).

During sequential compound fusion, the half-width (full width at half maximum) of the second Ω_{PH} (390 ± 38 nm, n = 23 Ω_{PH}) was similar to that (383 ± 22 nm, n = 23 Ω_{PH}) of the first Ω_{PH} (e.g., Fig. 1D), suggesting similar vesicle sizes for single and sequential compound fusion. Preformed Ω_{PH} (e.g., Fig. 1E, left images) has been characterized with STED XZ plane microscopy and electron microscopy (EM) (*25*). It is likely from previous fusion events that maintained a Ω shape, the so-called Ω-stay fusion or stay-fusion reported in recent studies (*21*–*24*, *28*). Supporting this possibility, the second fusion may occur ~20 to 85 s after the first fusion during sequential compound fusion (e.g., fig. S1, n = 4). Thus, on-preformed-Ω fusion may reflect sequential compound fusion with a prolonged delay.

Observing sequential compound release and release on preformed Ω-profile in real time

STED imaging of PH_G and A532 revealed the membrane dynamics, but not the vesicular content release dynamics. To demonstrate release dynamics, we loaded vesicles with fluorescent false neurotransmitter FFN511, a substrate for vesicle monoamine transporter, via bath application (Fig. 2A) (*33*). FFN511-loaded vesicles near or docked at the plasma membrane were observed in resting conditions (Fig. 2A) (*23*, *24*). Repeated STED imaging of PH_G and FFN511 at the XZ plane revealed decrease in FFN511 spot fluorescence (F_{FFN}) and simultaneous appearance of Ω_{PH} at the same spot, reflecting fusion-generated Ω_{PH} that releases FFN511 (Fig. 2, B to D). FFN511-releasing spots may mediate (i) single vesicle fusion, reflected as fusion on flat plasma membrane (Fig. 2B, n = 153, and movie S3); (ii) sequential compound fusion, reflected as fusion on flat plasma membrane to generate the first Ω_{PH}, followed on the first Ω_{PH}'s top or side by the second fusion that released FFN511 and created the second Ω_{PH}, forming an 8-shaped structure with the first Ω_{PH} (Fig. 2C, n = 11, and movie S4); or (iii) on-preformed-Ω fusion, reflected as fusion on preformed Ω_{PH} to form a PH_G-labeled 8-shaped structure (n = 31; Fig. 2D and movie S5).

During compound fusion (second fusion of sequential compound fusion) or on-preformed-Ω fusion, FFN511 fluorescence decrease was accompanied by a transient increase in FFN511 fluorescence at the first Ω_{PH} (for sequential compound fusion) or preformed Ω_{PH} (Fig. 2C, third FFN511 image; see also Fig. 3I, second FFN511 image). This result may reflect diffusion of FFN511 from the fusing vesicle to the already fused vesicle cavity before diffusing out to the bath solution. We did not observe this increase in every event

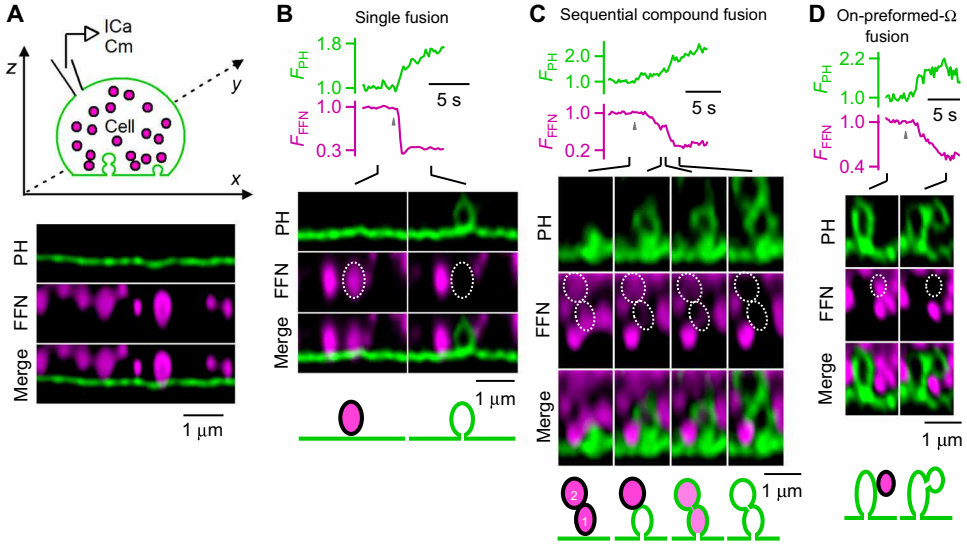

Fig. 2. Real-time visualization of sequential compound release and release on preformed Ω-profiles. (**A**) Setup drawing. The cell's membrane is labeled with PH_G (green), and vesicles are preloaded with FFN511 (magenta). ICa and Cm (capacitance) are recorded from the whole-cell pipette. (**B** to **D**) F_{PH}, FFN511 spot fluorescence (F_{FFN}), and STED XZ plane images at times indicated with lines showing release of FFN511 for single vesicle fusion (B), sequential compound fusion (C; vesicles 1 and 2 are circled), and on-preformed-Ω fusion (D). (C) Third column images show the instant of FFN511 release from vesicle 2, causing a transient increase in FFN511 fluorescence in vesicle 1.

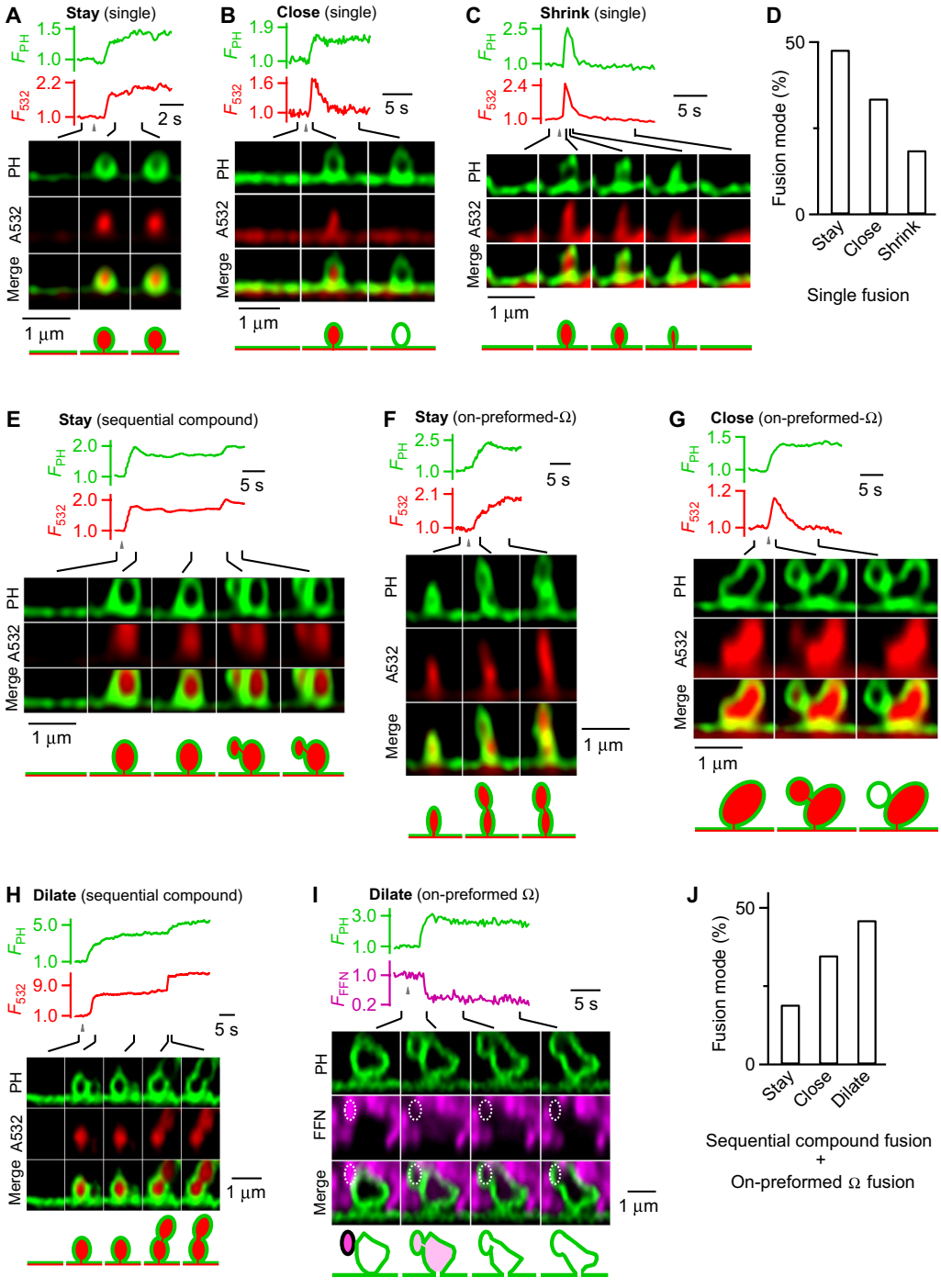

Fig. 3. Pore dynamics of compound and on-preformed-Ω fusion: stay, close, or dilate. (**A** to **C**) F_{PH}, F_{532} (strongly excited), and sampled images for three modes of single vesicle fusion induced by depol$_{1s}$ (grey triangle). (A) Stay-fusion, reflected as abrupt spot F_{532} and F_{PH} increase after fusion, which remained elevated during the recording time. (B) Close-fusion, reflected as abrupt spot F_{532} and F_{PH} increase, followed by F_{532} decay while F_{PH} remained unchanged or decayed with a delay, due to pore closure that prevented bath fluorescent A532 from exchanging with bleached A532 caused by strong and repeated excitation. (C) Shrink-fusion, reflected as abrupt spot F_{532} and F_{PH} increase followed by parallel Ω_{PH} and A532 spot shrinking, as well as parallel decreases in F_{532} and F_{PH}. (**D**) Stay-, close-, and shrink-fusion percentage for single vesicle fusion (247 events, 212 cells). (**E** and **F**) F_{PH}, F_{532}, and sampled images showing stay-fusion for compound fusion (E, second fusion event of the sequential compound fusion) and for on-preformed-Ω fusion (F), as induced by depol$_{1s}$ (gray triangle). (**G**) F_{PH}, F_{532}, and sampled images showing close-fusion for on-preformed-Ω fusion. The stimulation was depol$_{1s}$ [gray triangle, also applies to (H) and (I)]. (**H**) F_{PH}, F_{532}, and sampled images showing dilation of the fusion pore during compound fusion (pore dilation refers to second vesicle fusion). (**I**) F_{PH}, F_{511}, and sampled images showing dilation of the fusion pore during on-preformed-Ω fusion. Second column images show the instant of FFN511 release (from dotted vesicle), causing a transient increase in FFN511 fluorescence in the preformed Ω. (**J**) Percentage of stay-fusion, close-fusion, and pore dilation for compound (second vesicle) and on-preformed-Ω fusion ($n = 89$ events). Data from sequential compound fusion ($n = 23$ events) and on-preformed-Ω fusion ($n = 66$ events) were pooled together.

(observed in 22 of 42 events), likely due to low signal-to-noise ratios, FFN511 release faster than our imaging frequency, and/or FFN511 release too slow to increase FFN511 concentration above the detection limit in the already fused vesicle. In summary, results shown in Figs. 1 and 2 established the concept of sequential compound fusion and on-preformed-Ω fusion by demonstrating their vesicular positions, content release, and vesicular membrane structural changes in real time.

Pore behaviors of compound and on-preformed-Ω fusion: Stay, close or dilate

Once a fusion pore is established, the fusion pore may stay the same, expand, or close, and the fused Ω-shaped vesicular membrane profile may stay at the plasma membrane, merge with the plasma membrane, or reform vesicles via pore closure (*2*, *6*, *7*). Real-time observation of the membrane dynamics of sequential compound fusion and on-preformed-Ω fusion provided us a unique opportunity to reveal their pore behaviors, which had not been studied before. In the following, we presented the pore behaviors of single vesicle fusion first, and then compound fusion or on-preformed-Ω fusion.

As previously characterized in chromaffin cells [for details, see (*22*, *23*, *24*)], Ω_{PH} in single vesicle fusion may maintain an open pore (stay-fusion; Fig. 3A), close its pore at ~0.05 to 30 s later (close-fusion; Fig. 3B), or shrink to merge with the plasma membrane (shrink-fusion; Fig. 3C; summarized in Fig. 3D). Here, close-fusion was detected as A532 fluorescence (F_{532}, strongly excited) dimming due to pore closure that prevented bath fluorescent A532 from exchanging with bleached A532, while PH_G fluorescence (F_{PH}; weakly excited) sustained or decayed with a delay that reflected PI(4,5)P_2 conversion into PI(4)P and/or vesicle pinch off (Fig. 3B); stay-fusion was detected as sustained F_{532} and F_{PH} (Fig. 3A), and shrink-fusion, Ω_{PH} shrinking with parallel decreases of F_{532} and F_{PH} (Fig. 3C) (*23*, *24*, *34*).

Compound fusion (second fusion of sequential compound fusion) and on-preformed-Ω fusion may (i) remain unchanged with an open pore, reflected as sustained F_{532} and F_{PH} (Fig. 3, E and F, and movie S6), analogous to single vesicle's stay-fusion (Fig. 3A); (ii) close its pore at ~0.05 to 30 s later, reflected as F_{532} decay while F_{PH} sustained or decayed with a delay (Fig. 3G, movie S7), analogous to single vesicle fusion's close-fusion (Fig. 3B); or (iii) dilate its pore until the 8-shape was converted to a large elongated or round Ω-shape (e.g., Fig. 3, H and I; Fig. 3J shows their percentages; movies S2 and S8).

Unlike single vesicle fusion in which shrink-fusion mediates the merge of the fusing vesicle with the plasma membrane (*21*, *24*), compound or on-preformed-Ω fusion involves pore dilation, which formed an 8-shaped structure with a large pore between two ring-like structures (Fig. 3, H to J), reflecting the merge of the fusing vesicle membrane with the existing Ω-profile membrane. We did not observe shrink-fusion during compound or on-preformed-Ω fusion. We termed pore closure during compound or on-preformed-Ω fusion (e.g., Fig. 3G) compound kiss-and-run, a new form of kiss-and-run not reported previously.

Sequential compound fusion mediates desynchronized multivesicle release at a release site

By definition, sequential compound fusion should generate desynchronized, multivesicular release from the same release site. Here, we provided quantification of FFN511 release dynamics to support this prediction. We found that the 20 to 80% FFN511 fluorescence decay time was similar between the second and the first fusion event Ω_{PH} during sequential compound fusion (Fig. 4, A and B), suggesting that sequential compound fusion releases vesicular contents as efficiently as single vesicle fusion. However, the second fusion appeared at ~0.2 to 85 s after the first fusion (e.g., Figs. 1D, 2C, and 4A; summarized in Fig. 4C), indicating that sequential compound fusion generates desynchronized multivesicle release from single release sites. Given that the first fusion occurred mostly during and within ~1 s after $depol_{1s}$ (Fig. 4C), the first fusion reflected synchronized release. The various time delays of the second fusion (Fig. 4C) thus reflected asynchronous release. We concluded that sequential compound fusion contributes to the generation of desynchronized multivesicular release and asynchronous release.

Confocal XY plane imaging of compound and on-preformed-Ω fusion

STED imaging at the XZ plane revealed sequential compound and on-preformed-Ω fusion (Figs. 1 to 4). This finding was further supported by two sets of evidence obtained with more conventional techniques, XY plane confocal imaging, and EM described in the following two sections.

For confocal imaging at the XY plane, a technique many research laboratory can access to, we used three probes (*25*): (i) PH_G overexpressed to label plasma membrane, (ii) FFN511 preloaded to vesicles to indicate vesicle fusion and content release, and (iii) Atto 655 (A655; 30 μM, strongly excited) in the bath solution to fill and thus label fusing vesicles. We induced vesicle fusion with $depol_{1s}$ while performing confocal XY plane imaging of PH_G, A655, and FFN511 every 40 to 80 ms at a fixed Z plane ~100 to 200 nm above the cell-bottom membrane (Fig. 5A).

Single vesicle fusion was detected as FFN511 spot fluorescence (F_{FFN}) decrease with F_{PH} and A655 spot fluorescence (F_{655}) increase, due to FFN511 release and diffusion of PH_G and A655 from the plasma membrane and the bath into the fusion-generated Ω-profile, forming PH_G rings (or spots) and A655 spots (Fig. 5B) [for details, see (*23*, *24*)]. In 27 of 2030 fusion events (52 cells), a nearby FFN511-loaded vesicle fusion took place, resulting in the FFN511 spot's F_{FFN} decrease, F_{PH} increase, F_{655} increase, and formation of a PH_G-labeled ring (Fig. 5C, second column images). This ring and the adjacent fusion-generated PH_G-labeled ring formed an 8-shaped PH_G-labeled structure (Fig. 5C, third column images), which was subsequently evolved into a large oval-shaped structure (Fig. 5C, fourth column images), because of dilation of the pore between the two PH_G-labeled rings. These vesicular structural changes reflected sequential compound fusion with pore dilation, similar to those observed with STED XZ plane imaging (e.g., Fig. 3H).

We also observed FFN511-loaded vesicle fusion on the adjacent preformed Ω (PH_G-labeled ring; Fig. 5D, first column images), resulting in the FFN511 spot's F_{FFN} decrease, F_{PH} increase, F_{655} increase, and formation of a PH_G-labeled ring, which, together with the preformed PH_G-labeled ring, formed an 8-shaped structure (Fig. 5D, second column images). The PH_G-labeled 8-shaped structure was subsequently evolved into a large oval-shaped structure because of dilation of the pore between the fusing vesicle and the preformed Ω-profile (25 of 2030 fusion events, 52 cells; Fig. 5D). These results reflect fusion on preformed Ω with pore dilation, similar to those observed with STED XZ plane imaging (e.g., Fig. 3I).

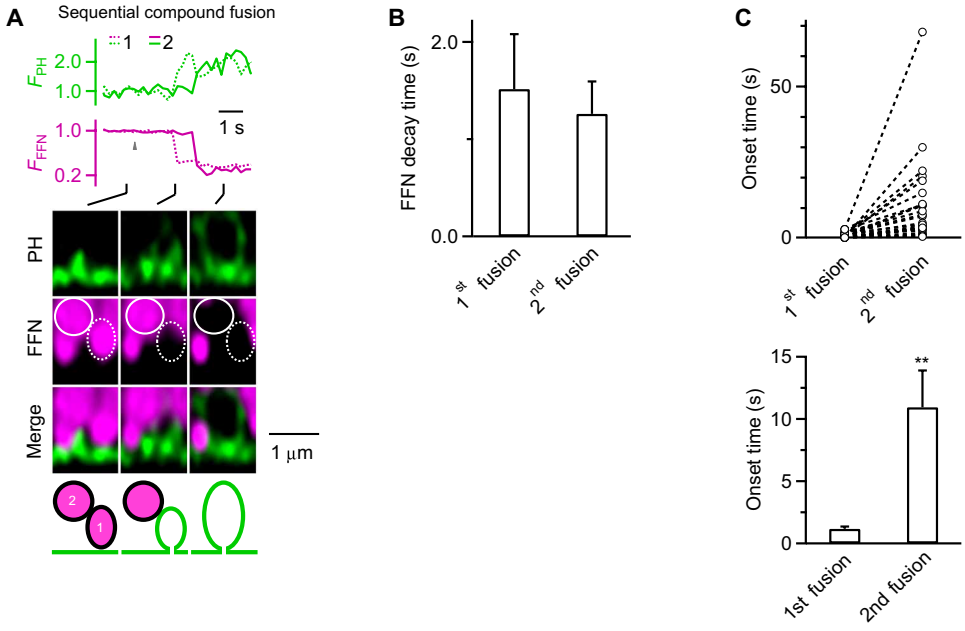

Fig. 4. Sequential compound fusion releases contents efficiently but generates desynchronized multivesicular release and asynchronized release at single release sites. (**A**) F_{PH}, F_{FFN}, and sampled images of the first (dotted circle, dotted trace) and the second (solid circle, solid trace) fusion for a sequential compound fusion event observed after $depol_{1s}$ (grey triangle). (**B**) The 20 to 80% F_{FFN} decay (release) time (means + SEM) for the first and second fusion during sequential compound fusion (11 events, 11 cells under PH_G/FFN511 imaging). No significant difference was found (paired *t* test, $P = 0.712$). (**C**) Upper: The onset time of the first and the second fusions during sequential compound fusion (23 events, 23 cells under PH_G/A532 imaging). One fusion per circle; dashed lines connect two fusion events from the same sequential compound fusion event. Onset time 0 refers to the onset of $depol_{1s}$. The data show various delays of the second fusion event. Lower: Mean onset (+ SEM, $n = 23$) of the first and the second fusions during sequential compound fusion showing a significant delay of the second fusion event (**$P < 0.01$, paired *t* test). Upper and lower panels are from the same dataset.

XY plane confocal imaging may substantially underestimate sequential compound fusion and on-preformed-Ω fusion. This is because it must fulfill three requirements: (i) Compound or on-preformed-Ω fusion is on the side of the already fused $Ω_{PH}$ so that it can be visualized at the XY plane (e.g., Fig. 2D), (ii) PH_G-labeled $Ω_{PH}$ is large enough to be resolved with confocal microscopy, and (iii) compound or on-preformed-Ω fusion must involve pore dilation resolvable with confocal microscopy. Nevertheless, XY plane confocal imaging further supports our STED XZ plane observation of sequential compound fusion and on-preformed-Ω fusion.

Electron microscopic observation of plasma membrane profiles

Chromaffin cells were incubated in 70 mM KCl solution for 1.5 min, after which chemical fixation or high-pressure freezing was applied for EM examination. In 2200 cell cross sections examined with EM, we found 10 plasma membrane profiles appearing as 8-shaped structures with a large pore in between (Fig. 5E), 4 membrane profiles appearing as prolonged cylinder-like (>600 nm) structures (e.g., Fig. 5F, left), and 11 membrane profiles appearing as large vesicles (>600 nm, e.g., Fig. 5F, right). These structures were similar to sequential compound or on-preformed-Ω fusion structures observed in live cells (e.g., Figs. 1E; 2C; 3, H and I; and 4A, and fig. S1). They were likely underestimated because (i) the EM cross section has to cut through both the pore between the first and the second fusing vesicles and the pore between the compound vesicle and the plasma membrane, and (ii) such a structure has to be maintained until the time of fixation. These EM structures support compound fusion and on-preformed-Ω fusion, although alternative explanations could not be fully excluded because of the lack of membrane dynamics information inherent to the EM approach.

DISCUSSION

The present work firmly established the concept of sequential compound fusion and compound kiss-and-run by directly visualizing their dynamics of membrane structural changes, fusion pore opening and closure, and vesicular content release in live cells. Sequential compound fusion and compound kiss-and-run may contribute to mediate various steps and modes of exo- and endocytosis, such as vesicle docking and priming, rapid establishment of functional release sites, desynchronized multivesicular release, asynchronous release, and endocytosis that recycles vesicles to sustain release, as discussed below.

Vesicle fusion must involve vesicle movement toward the well-established plasma membrane release sites, docking at release sites, and vesicular V-SNARE and plasma membrane T-SNARE binding that may prime docked vesicles for release (*4*, *8*). Our findings suggest modifying this concept by including a new mechanism—rapid assembly of release sites at the just fused vesicular Ω-shaped membrane profile. Such a rapid release site assembly and subsequent vesicle docking/priming may save vesicles from spending energy to travel one-vesicle-length of distance for docking at the original flat plasma membrane release site. Release site assembly may involve diffusion of T-SNARE from the plasma membrane to the fusion-generated Ω-profile; docked vesicle priming may involve T-SNARE

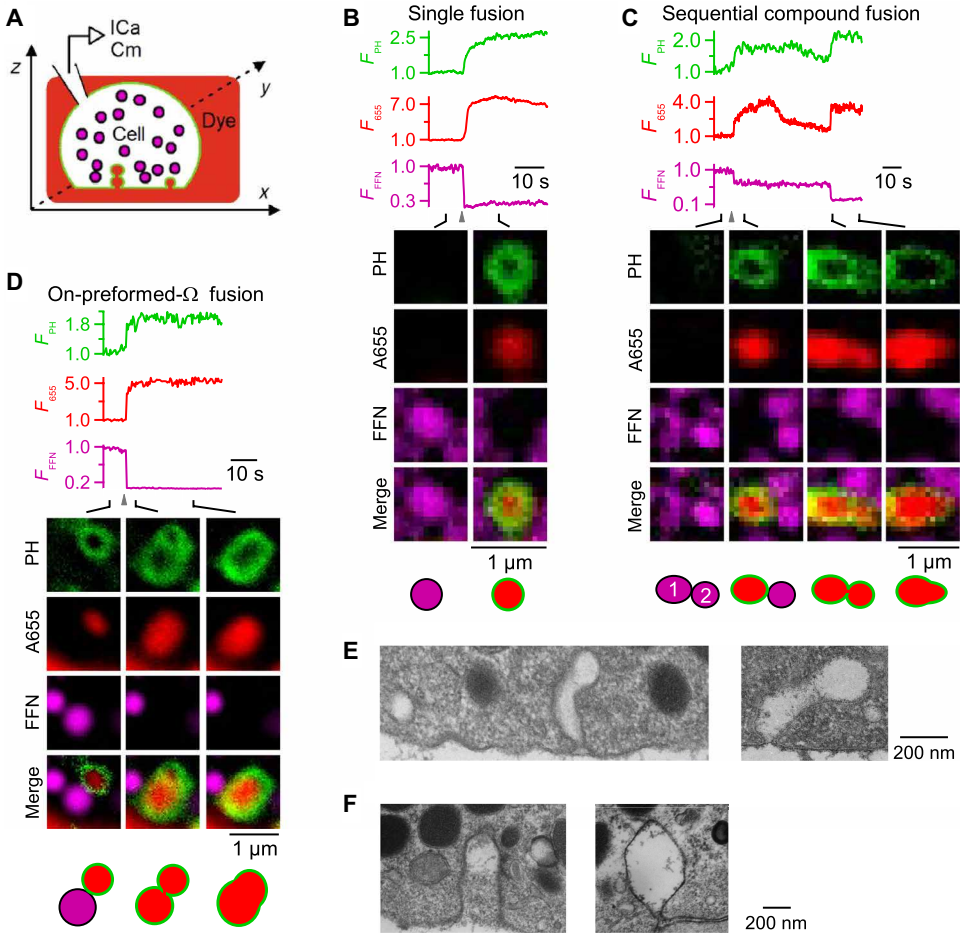

Fig. 5. Confocal imaging at the XY plane and electron microscopy support compound and on-preformed-Ω fusion. (**A**) Setup drawing: The cell's membrane is labeled with PH_G (green), vesicles are preloaded with FFN511 (magenta), and the bath solution includes A655 (red). ICa and Cm (capacitance) are recorded from the whole-cell pipette. (**B** to **D**) F_{PH} (normalized to baseline), A655 spot fluorescence (F_{655}, normalized to baseline), F_{FFN}, and confocal XY plane images at times indicated with lines showing single vesicle fusion (B), sequential compound fusion (C, first and second vesicles are labeled), and on-preformed-Ω fusion (D). The stimulation was $depol_{1s}$ (gray triangle). Drawings of FFN511-containing vesicles (magenta) and fusing vesicles (green membrane) containing A655 (red) are shown at the bottom. (**E** and **F**) Electron microscopic images of 8-shaped profiles (E), long cylinder-like profile (F, left), and large Ω-shaped profile (F, right) at chromaffin cell plasma membrane. Cells were in 70 mM KCl solution for 1.5 min before fixation.

binding with V-SNARE of the docked vesicle (*35*). These processes may take time (*35*), explaining the prolonged release interval of sequential compound fusion that produces asynchronous release.

Multivesicular release from single release sites enhances synaptic strength, synaptic reliability, and the dynamic range of synaptic plasticity and neuromodulation at many synapses (*1*). Multivesicular release is also observed in endocrine cells. In pancreatic β cells that release insulin to control blood glucose level relevant to diabetes, multivesicular release from single release sites, proposed to be caused by compound fusion, has been suggested to augment glucose-induced insulin secretion (*36*). Multivesicular release in adrenal chromaffin cells could, in principle, enhance animal's "fight or flight" response by enhancing the capacity of release from limited release sites. Despite the importance of multivesicular release, its underlying mechanisms are poorly understood (*1*). Sequential compound fusion, the concept of which has been established here with direct observation of membrane and release dynamics, readily explains how single release sites can support multivesicular release, particularly the desynchronized multivesicular release. If the release interval of sequential compound fusion is minimal, it may also explain the coordinated or simultaneous multivesicular release widely reported at single release sites (*1*, *11*). By contributing to the generation of multivesicular release, sequential compound fusion may enhance the precise and efficient firing information transfer at synapses (*9*, *32*), augment glucose-induced insulin secretion in pancreatic β cells, and increase release in adrenal chromaffin cells for the fight or flight response. Compound kiss-and-run may thus contribute to recycle fused vesicles in the enhanced release conditions.

While depolarization-evoked release is mostly synchronized, asynchronous release lasting much longer than the brief depolarization also takes place in many excitable cells, which may transfer a brief presynaptic firing burst into a prolonged postsynaptic firing burst at synapses (*8*). The differences in the mechanisms underlying asynchronous and synchronous release remain not well understood. Different calcium sensors with different calcium affinity have been suggested (*8*). Sequential compound fusion evidently generates a delay

in releasing the second vesicle (Fig. 4), providing a previously unidentified mechanism contributing to the generation of asynchronous release.

The delay of the second release during sequential compound fusion may be due to assembly of release sites at the just fused vesicular Ω-shaped membrane profile. It is possible that a different calcium sensor with a higher calcium affinity is responsible for compound fusion. The molecular mechanisms underlying compound fusion and kiss-and-run remain largely unexplored. We propose that similar to single vesicle fusion and kiss-and-run observed in chromaffin cells, they may involve (i) core exocytosis proteins such as SNARE proteins and calcium sensor synaptotagmin to mediate compound fusion (*4*, *37*–*39*), (ii) hemifusion and hemi-to-full fusion as the membrane pathway to fusion pore opening (*22*), (iii) F-actin and membrane tension for fusion pore expansion and dilation (*23*, *40*), and (iv) dynamin for mediating compound kiss-and-run (*21*–*23*). It would be of great interest to verify this proposal in the future.

Compound kiss-and-run reported here is a new mode of exo-endocytosis that retrieves vesicles undergoing sequential compound fusion. It may explain the electron microscopic observation of 8-shaped (or sausage-shaped) structures that are otherwise interpreted as different mechanisms, such as vesicle budding or cytosol vesicle-vesicle fusion. We suggest modifying current models of secretory vesicle endocytosis (*2*, *41*) by including compound kiss-and-run as a new mode of endocytosis. This mode of endocytosis may enhance the endocytic capacity of the cell during repetitive stimulation, in which sequential compound fusion may occur frequently.

While obtained from chromaffin cells containing large dense-core vesicles, our findings are most likely applicable to neurons for two reasons. First, similar to neurons, chromaffin cells are excitable cells with a neuronal origin and with similar calcium-, synaptotagmin-, SNARE-, and dynamin-dependent exo- and endocytosis (*2*, *6*). Second, neurons contain large dense-core and small clear-core vesicles, both of which may maintain an Ω-shape after fusion (*28*, *42*–*44*), the prerequisite for mediating sequential compound fusion. Direct visualization is eventually needed to prove sequential compound fusion and kiss-and-run in neurons, although resolving rapid membrane dynamics of small (~30 to 50 nm) synaptic vesicles may require technical advancements in the future.

Cytosolic vesicle-vesicle fusion is the first form of compound fusion being proposed, based on the observation of (i) cytosolic 8-shaped or sausage-like vesicular structures and (ii) capacitance jumps and synaptic miniature currents (quantal response) too large for single vesicle fusion in nonexcitable and excitable cells, such as pancreatic acinar cells, eosinophils, mast cells, calyx-type, and ribbon-type synapses (*29*, *31*, *37*, *45*–*48*). However, direct observation of the membrane transformation during vesicle-vesicle fusion, which can fully establish the concept of vesicle-vesicle fusion, is still missing. Similar to vesicle-vesicle fusion, sequential compound fusion was suggested in nonexcitable cells based on the observation of (i) sequential release of LysoTracker Green loaded into the giant (~1 to 5 μm) granules in eosinophils (*29*) and (ii) sequential generation of extracellular dye–loaded giant tube-like structures from the plasma membrane into the cytosol in acinar cells (*30*). However, these studies could not fully exclude the possibility that the apparently cytosolic LysoTracker Green–loaded giant vesicles could dock and release at the plasma membrane out of the focal plane (instead of release at the fused Ω-shaped membrane) or that the extracellular dye–loaded structure reflects endocytic membrane invagination (content release is not imaged simultaneously). Because of the indirect evidence and the lack of evidence showing direct, simultaneous membrane structural changes, fusion pore dynamics, and release dynamics of sequential compound fusion in live cells, the concept of sequential compound fusion is not fully established in nonexcitable cells (*2*). Its potential application to excitable cells is thus being neglected. The present work provided the missing evidence required to fully establish the concept of sequential compound fusion—the dynamics of membrane transformation, fusion pore, and content release. Furthermore, we link this concept to a new endocytic mode, compound kiss-and-run, and extend these concepts to excitable cells that release much smaller vesicles much more rapidly. Thus, sequential compound fusion and compound kiss-and-run may be a widespread exo-endocytosis mode used by excitable and nonexcitable cells to mediate diverse functions such as neuronal communication, fight or flight response, regulation of blood glucose level relevant to diabetes, immune responses, and viral entry and budding (*1*, *2*). In addition, the technique we used here opens the door to study the functions and mechanisms of sequential compound fusion and compound kiss-and-run in live cells.

MATERIALS AND METHODS

Chromaffin cell culture

We prepared primary bovine adrenal chromaffin cell culture as described previously (*21*). Fresh adult (21 to 27 months old) bovine adrenal glands (from a local abattoir) were immersed in prechilled Locke's buffer on ice containing NaCl, 145 mM; KCl, 5.4 mM; Na_2HPO_4, 2.2 mM; NaH_2PO_4, 0.9 mM; glucose, 5.6 mM; Hepes, 10 mM (pH 7.3, adjusted with NaOH). Glands were perfused with Locke's buffer, then infused with Locke's buffer containing collagenase P (1.5 mg/ml; Roche), trypsin inhibitor (0.325 mg/ml; Sigma-Aldrich), and bovine serum albumin (5 mg/ml; Sigma-Aldrich), and incubated at 37°C for 20 min. The digested medulla was minced in Locke's buffer and filtered through a 100-μm nylon mesh. The filtrate was centrifuged (48*g*, 5 min), resuspended in Locke's buffer, and recentrifuged until the supernatant was clear. The final cell pellet was resuspended in prewarmed Dulbecco's modified Eagle's medium (Gibco) supplemented with 10% fetal bovine serum (Gibco).

Electroporation and plating

Cells were transfected by electroporation using the Basic Primary Neurons Nucleofector Kit (Lonza), according to the manufacturer's protocol, and plated onto glass coverslips with mouse Laminin coating over poly-D-lysine layer (Neuvitro). The cells were incubated at 37°C with 9% CO_2 and used within 5 days.

Plasmids and fluorescent dyes

The PH-EGFP (phospholipase C delta PH domain attached with EGFP) was obtained from T. Balla. PH-mNeonGreen construct was created by replacing the EGFP tag of PH-EGFP with mNeonGreen (Allele Biotechnology) (*49*). Both PH-EGFP and PH-mNeonGreen are abbreviated as PH_G. For A532 (Sigma-Aldrich) imaging, A532 concentration in the bath solution was 30 μM. For FFN511 (Abcam) imaging, cells were bathed with FFN511 (5 to 10 μM) for 10 min, and imaging was performed after washing out FFN511 in the bath solution. For A655 (Sigma-Aldrich) imaging, A655 concentration in the bath solution was 30 μM.

Many previous studies suggest that $PI(4,5)P_2$ is important for exocytosis and endocytosis (*50*–*56*). Four sets of evidence suggest that overexpression of PH_G, which binds and labels $PI(4,5)P_2$, does

not substantially inhibit exo- or endocytosis induced by $depol_{1s}$ in bovine adrenal chromaffin cells—the experimental condition of the present work. First, confocal imaging of PH_G and A655 at the XY plane with a fixed *Z* plane ~100 nm above the cell bottom showed that $depol_{1s}$ induced 25.1 ± 3.9 fusion spots per cell (n = 16 cells; fig. S2) [see also Fig. 1, C to F, in (*22*)]. When PH_G was replaced with GFP tagged to Lyn kinase's myristoylation and palmitoylation sequence (PM-GFP), which also labels the plasma membrane inner leaflet but does not bind $PI(4,5)P_2$ (*57*), $depol_{1s}$ induced 16.0 ± 4.8 fusion spots per cell (n = 7 cells; fig. S2) [see also Fig. 1H in (*22*)]. This number (16.0 ± 4.8) was clearly not significantly higher than that (25.1 ± 3.9) obtained in cells overexpressed with PH_G (fig. S2), indicating that PH_G overexpression does not significantly reduce fusion events induced by $depol_{1s}$. Furthermore, the percentage of full fusion and detectable hemi- and then full fusion were not significantly different between PH_G-overexpressed and PM-GFP–overexpressed cells [see Fig. 1, G and I, in (*22*). Second, after $depol_{1s}$, the capacitance jump and subsequent decay time course in cells overexpressed with PH_G (n = 77 cells) were similar to those without PH_G overexpression (n = 52 cells) [see fig. S7A in (*25*)], suggesting that PH_G overexpression does not affect whole-cell exo- and endocytosis induced by $depol_{1s}$. Third, the percentage of cells showing no endocytosis, compensatory endocytosis, and overshoot endocytosis in cells overexpressed with PH_G (n = 77) were similar to those without PH_G overexpression (n = 52) [see fig. S7B in (*25*)], suggesting that PH_G overexpression does not affect endocytosis. Fourth, the percentage of preformed Ω-profile pore closure measured with A655 imaging in cells overexpressed with PH_G (n = 20 cells) was similar to that without PH_G overexpression (n = 20 cells) [see fig. S7C in (*25*)], suggesting that PH_G overexpression does not affect fission pore closure induced by $depol_{1s}$. We also observed similar percentages of close-fusion and non–close-fusion in cells with or without PH_G overexpression (*21*, *22*).

An early pioneering study showed that overexpression of PH domain (phospholipase C delta PH domain) reduced exocytosis by ~50% after application of barium, digitonin that permeabilizes the cell, or a 50-ms depolarization (*50*). We did not observe a reduction of exocytosis after $depol_{1s}$, likely because (i) $depol_{1s}$ may induce a much higher calcium influx in a brief 1-s time window to evoke a saturated amount of release (e.g., depletion of the readily releasable pool), which may overcome partial inhibition by the PH domain binding with only a fraction of $PI(4,5)P_2$ molecules, and (ii) a potentially less degree of PH domain overexpression may only bind to a smaller fraction of $PI(4,5)P_2$ molecules.

Electrophysiology

At room temperature (20° to 22°C), whole-cell voltage clamp and capacitance recordings were performed with an EPC-10 amplifier together with the software lock-in amplifier (PULSE, HEKA, Lambrecht, Germany) (*21*, *58*). The holding potential was −80 mV. For capacitance measurements, the frequency of the sinusoidal stimulus was 1000 to 1500 Hz with a peak-to-peak voltage ≤50 mV. The bath solution contained 125 mM NaCl, 10 mM glucose, 10 mM Hepes, 5 mM $CaCl_2$, 1 mM $MgCl_2$, 4.5 mM KCl, and 20 mM tetraethylammonium (pH 7.3) adjusted with NaOH. The pipette (2 to 4 megohms) solution contained 130 mM Cs-glutamate, 0.5 mM Cs-EGTA, 12 mM NaCl, 30 mM Hepes, 1 mM $MgCl_2$, 2 mM adenosine 5′-triphosphate (ATP), and 0.5 mM guanosine 5′-triphosphate (GTP) (pH 7.2) adjusted with CsOH. These solutions pharmacologically isolated calcium currents.

For stimulation, we used a 1-s depolarization from the holding potential of −80 to +10 mV ($depol_{1s}$). We used this stimulus because it induces robust exo-endocytosis as reflected in capacitance recordings (Fig. 1A) (*21*, *59*). In a fraction of experiments during FFN511 imaging, we used 10 pulses of 400-ms depolarization from −80 to +10 mV at 2 Hz, which evoked more fusion events.

STED imaging

STED images were acquired with a Leica TCS SP8 STED 3× microscope that is equipped with a 100 × 1.4 numerical aperture HC PL APO CS2 oil immersion objective and operated with the LAS-X imaging software. Excitation was with a tunable white light laser, and emission was detected with hybrid detectors. In time-gated STED mode, PH-EGFP and A532 were sequentially excited at 470 and 532 nm, respectively, with the 592-nm STED depletion beam, and their fluorescence was collected at 475 to 525 nm and 540 to 587 nm, respectively. PH-mNeonGreen and A532 were sequentially excited at 485 and 540 nm, respectively, with the 592-nm STED depletion beam, and their fluorescence was collected at 490 to 530 nm and 545 to 587 nm, respectively. PH-mNeonGreen and FFN511 were sequentially excited at 505 and 442 nm, respectively, with the 592-nm STED depletion beam, and their fluorescence was collected at 510 to 587 nm and 447 to 490 nm, respectively.

The excitation power for A532 was 10% of the maximum, at which fluorescent A532 can be bleached within a few seconds. This feature was used to distinguish whether the fusion pore is closed or not, because pore closure prevents bleached A532 (caused by strong excitation) from exchange with fluorescent A532 in the bath, resulting in A532 spot fluorescence decay (*21*–*23*). In contrast, an open pore would not cause A532 spot fluorescence decay, because an open pore allows for continuous exchange of bleached A532 in the Ω-profile with fluorescent A532 in the bath (*21*–*23*).

STED imaging generally causes more photobleaching and phototoxicity. Severe phototoxicity could cause loss of the whole-cell giga seal during patch-clamp recording (*21*). In general, we avoided severe phototoxicity by applying only one $depol_{1s}$ and imaging for ~1 to 2 min per cell. With this setting, we have not noticed substantial differences in the exo- and endocytosis properties obtained under confocal and STED imaging conditions (*21*, *22*). For imaging of PH_G and A532, continuous exchange of bleached PH_G or A532 with fluorescent ones from nonimaging areas lessened the photobleaching problem.

STED scanning modes

STED images were acquired at the cell bottom at the XZ plane (perpendicular to the coverslip) with the *Y* axis location fixed at about the cell center (Figure 1A). We repeated these scannings every 26 to 300 ms at 15 nm per pixel in an XZ area of 19.4 μm × 0.7 to 2.5 μm (*23*).

The STED resolution for imaging PH_G (PH-EGFP or PH-mNeonGreen) in our conditions was ~60 nm on the microscopic *X* and *Y* axes (parallel to cell-bottom membrane or coverslip) and ~150 to 200 nm on the microscopic *Z* axis. STED images were deconvolved using Huygens software (Scientific Volume Imaging).

Detection of fusion pore closure

During STED imaging of PH_G and A532, fusion pore closure was detected as A532 fluorescence (F_{532}, strongly excited) dimming due to pore closure that prevented bath fluorescent A532 from exchanging with bleached A532, while PH_G fluorescence (F_{PH}, weakly excited) sustained (within our recording time of ~1 to 2 min) or decayed

with a delay that reflected PI(4,5)P_2 conversion into PI(4)P and/or vesicle pinch off (*21*–*23*, *25*). Four sets of data described below further support this bleaching method that detects fusion pore closure.

First, upon fusion pore closure detected with the bleaching method, bath application of an acid solution could not quench the pH-sensitive vesicle-associated membrane protein 2 (VAMP2) attached with EGFP or VAMP2-pHluorin expressed at the fused vesicle, suggesting that fusion pore closure detected with the bleaching method prevents the exchange of H^+ and OH^-, the smallest molecules between the "closed" vesicle and the bath solution [see Fig. 9 in (*21*)] (*22*). This result confirms that the bleaching method can detect fusion pore closure that is impermeable to the smallest molecules such as H^+ and OH^-. In a pioneering study, this bleaching method has been used to detect fusion pore closure that takes minutes in pancreatic acinar cells (*34*).

Second, imaging of PH-mCherry and VAMP2-pHluorin (pH-sensitive fluorescent protein at the vesicular membrane) showed that vesicle fusion pore opening and closure, detected as VAMP2-pHluorin fluorescence increase and decay, were accompanied by PH-mCherry fluorescence increase, which may sustain or decay with a delay after VAMP2-pHluorin fluorescence decay [see extended data Fig. 6 in (*22*)]. In some fusion pore closure events, PH fluorescence decayed with a delay after fusion pore closure was detected with the bleaching method, indicating that PI(4,5)P_2 eventually may decay after fusion pore closure [see extended data Fig. 6 in (*22*)] [see Fig. 6B in (*25*)]. Our fluorescence imaging revealed that PI(4,5)P_2 is converted into PI(4)P with various delays after fusion pore closure [see extended data Fig. 7 in (*22*)]. Thus, PH_G fluorescence decay can be used to indicate a time after pore closure, whereas no decay of the PH_G fluorescence cannot be used to indicate an open fusion pore.

Third, fusion pore closure detected with the bleaching method (A532, A655, or A647 fluorescent decay while PH fluorescence sustains or decays with a delay) can be blocked by dynamin inhibitor dynasore, dynamin 1-K44A (dynamin dominant negative mutant) overexpression, or dynamin knockdown, all of which also block endocytosis detected with whole-cell capacitance measurements (*21*, *22*, *25*). This result suggests that fusion pore closure detected with the bleaching method depends on dynamin, the well-known guanosine triphosphatase (GTPase)–mediating fission.

Fourth, reconstruction of the whole-cell exo-endocytosis trace from each individual event of fusion pore opening, fusion pore closure, and fission pore closure detected with the bleaching method (A655 fluorescent decay while PH fluorescence sustains or decays with a delay) from single cells faithfully reproduces the corresponding cell's capacitance increase and decay in control and in the presence of dynamin inhibitors [see Figs. 6 and 7 in (*25*)]. This result further verifies our bleaching method that detects dynamin-dependent fusion and fission pore closure.

Confocal imaging at the XY plane

Imaging of PH_G, A655, and FFN511 was performed with an inverted confocal microscope (TCS SP5II, Leica, Germany, 100× oil objective, numerical aperture: 1.4). PH_G was excited by a tunable white light laser at 515 nm (laser power set at ~1 to 4 mW); A655 was excited by an HeNe laser at 633 nm (laser power set at ~12 to 15 mW); FFN511 was excited by an argon laser at 458 nm (laser power set at ~2 to 4 mW); their fluorescence was collected at 520 to 600 nm, 650 to 800 nm, and 465 to 510 nm, respectively. Confocal imaging area was ~70 to 160 μm^2 at the XY plane with a fixed *Z* axis focal plane ~100 to 200 nm above the cell-bottom membrane. Images were collected every 40 to 80 ms at 40 to 60 nm per pixel.

During confocal XY plane imaging of PH_G, A655, and FFN511 at the cell bottom, fusion was detected as FFN511 fluorescence (F_{FFN}) decrease with PH_G fluorescence (F_{PH}) and A655 fluorescence (F_{655}) increase. These changes reflect FFN511 release and PH_G/A655 spot formation by PH_G/A655 diffusion from plasma membrane/bath into fusion-generated Ω-profiles (*23*–*25*).

Data selection for confocal and STED imaging

For every cell recorded with a pipette under the whole-cell configuration, the data within the first 2 min at the whole-cell configuration were used, which avoided rundown of endocytosis (gradual disappearance of endocytosis) as previously reported under the whole-cell configuration for a long time (*21*, *60*). Cells expressed with PH_G were used for visualization of fusion events. The criteria for selecting PH_G-labeled Ω for analysis during XZ scanning are described in fig. S2 of (*23*).

Analysis of PH_G-labeled Ω-shaped profiles

STED images of PH-Ω were analyzed with ImageJ and LAS X (Leica). During XZ scanning, some $depol_{1s}$-induced PH-Ω-profiles were out of the Y focal plane, as the outline of the Ω-profile was vague or unclear [for details, (*23*)]. These out-of-focus Ω-profiles were not included for analysis.

Pores labeled with PH_G were identified on the basis of the image and the fluorescence intensity line profile [for details, see (*23*)]. We first identified the fluorescently labeled Ω-profiles with an open pore, the edge of which was continuous with the plasma membrane. The intensity line profile in the pore region should show a valley with a peak at least three times larger than the baseline fluctuation (SD) in the nonpore region [for details, see (*23*)]. The full width at half maximum of the valley of the intensity line profile across the pore was proportional to the pore diameter, as shown with simulation (*23*). Pore dilation of the fusing Ω_{PH} during sequential compound fusion or on-preformed-Ω fusion was judged with eyes.

Identification of stay-, close-, and shrink-fusion during repeated XZ plane STED imaging of PH_G/A532 was described in detail previously (*23*). During XZ plane imaging, A532 was excited at a high laser power so that fluorescent A532 can be bleached with a time constant of 1.5 to 3.5 s. Pore closure was identified as the gradual dimming of the A532 spot fluorescence to baseline during XZ plane PH_G/A532 imaging, while PH_G image remained unchanged or dimmed gradually without changing the Ω_{PH} size (*23*). A532 fluorescence dimming was not due to a narrow pore smaller than A532 molecule size because, after A532 spot dimming, bath application of an acid solution cannot quench the pH-sensitive VAMP2-EGFP or VAMP2-pHluorin overexpressed at the same spot, indicating that the spot is impermeable to H^+ or OH^-, the smallest molecules, and thus is closed (*21*, *22*).

Electron microscopy

Bovine chromaffin cells were either chemically fixed (on coverslips) or cryo-fixed (in suspension). Before fixation, cells were stimulated for 1.5 min using a solution containing 70 mM KCl, 60 mM NaCl, 10 mM glucose, 10 mM Hepes, 2 mM $CaCl_2$, and 1 mM $MgCl_2$ (pH 7.3). For chemical fixation, cells on coverslips were immersed in 2% glutaraldehyde, 2% paraformaldehyde, and 4% tannic acid in 0.1 M cacodylate buffer (pH 7.4) solution for 15 min, and then transferred into the same fixative without tannic acid for an additional 15 min. The cells were washed with a solution of 100 mM glycine in 0.1 M sodium cacodylate buffer (pH 7.3) for 1 min at room temperature

and then with 0.1 M sodium cacodylate. After postfixation in 1% OsO_4 for 1 hour on ice, the samples were dehydrated in ethanol series and embedded in Embed-812. During dehydration, the specimens were stained with 2% uranyl acetate in 70% ethanol for 30 min.

For cryo-fixation, cells in suspension were sedimented by gravity, and the medium was carefully removed. Approximately 0.5 µl of cell pellet was transferred to a 3-mm type A planchet with a depth of 200 µm precoated with dioleoylphosphatidylcholine lipids. The entire volume of the planchet was filled with the pellet solution. The type B planchet was placed on the top with the flat surface down to seal the assembly. The assembled specimen chamber was frozen using an EM ICE high-pressure freezing (Leica Microsystems). The frozen samples were transferred to cryovials under liquid nitrogen vapor and then to a precooled (−90°C) freeze substitution unit (EM AFS from Leica Microsystems). Freeze substitution was performed using a solution of 1% tannic acid in dry acetone for 24 hours followed by an exchange to a mixture of 2% uranyl acetate, 1% glutaraldehyde, and 3% H_2O in acetone for 21 hours. Then, the samples were washed three times for 1 hour each with precooled, dry acetone. We did not use OsO_4. Instead, we used tannic acid in combination with uranyl acetate. The temperature was slowly raised from −90° to −30°C in 96 hours (0.6°C/hour) and from −30° to 21°C in 36 hours (1.4°C/hour). Samples were separated from the planchets in acetone at room temperature. Infiltration and embedding with Embed-812 were then performed.

Ultrathin 60- to 70-nm sections from Embed-812 embedded specimens were cut with a diamond knife (Diatome) in an ultramicrotome UC7 (Leica Microsystems) and mounted onto mesh grids. Sections were counterstained with lead citrate for 5 min. Digital micrographs were acquired at 120 kV in either a JEOL JEM-200cx electron microscope equipped with a bottom-mounted AMT XR-100 CCD camera or a JEOL JEM1400 electron microscope equipped with a bottom-mounted AMT-BioSprint29L-ActiveVu camera.

Statistical tests

Data were expressed as means ± SEM. Replicates are indicated in results and figure legends. *N* represents the number of cells, fusion events, pores, or Ω-profiles as indicated in Results and figure legends. The statistical test used is *t* test. Although the statistics were performed on the basis of the number of cells, fusion events, pores, and Ω-profiles, each group of data was collected from at least four primary chromaffin cell cultures. Each culture was from at least two glands from one bovine.

SUPPLEMENTARY MATERIALS

Supplementary material for this article is available at https://science.org/doi/10.1126/sciadv.abm6049

View/request a protocol for this paper from *Bio-protocol*.

REFERENCES AND NOTES

1. S. Rudolph, M. C. Tsai, H. von Gersdorff, J. I. Wadiche, The ubiquitous nature of multivesicular release. *Trends Neurosci.* **38**, 428–438 (2015).
2. L. G. Wu, E. Hamid, W. Shin, H. C. Chiang, Exocytosis and endocytosis: Modes, functions, and coupling mechanisms. *Annu. Rev. Physiol.* **76**, 301–331 (2014).
3. R. S. Zucker, W. G. Regehr, Short-term synaptic plasticity. *Annu. Rev. Physiol.* **64**, 355–405 (2002).
4. R. Jahn, D. Fasshauer, Molecular machines governing exocytosis of synaptic vesicles. *Nature* **490**, 201–207 (2012).
5. E. Neher, What is rate-limiting during sustained synaptic activity: Vesicle supply or the availability of release sites. *Front Synaptic. Neurosci.* **2**, 144 (2010).
6. S. Sharma, M. Lindau, The fusion pore, 60 years after the first cartoon. *FEBS Lett.* **592**, 3542–3562 (2018).
7. C. W. Chang, C. W. Chiang, M. B. Jackson, Fusion pores and their control of neurotransmitter and hormone release. *J. Gen. Physiol.* **149**, 301–322 (2017).
8. P. S. Kaeser, W. G. Regehr, Molecular mechanisms for synchronous, asynchronous, and spontaneous neurotransmitter release. *Annu. Rev. Physiol.* **76**, 333–363 (2014).
9. C. Auger, S. Kondo, A. Marty, Multivesicular release at single functional synaptic sites in cerebellar stellate and basket cells. *J. Neuorsci.* **18**, 4532–4547 (1998).
10. J. Y. Sun, L. G. Wu, Fast kinetics of exocytosis revealed by simultaneous measurements of presynaptic capacitance and postsynaptic currents at a central synapse. *Neuron* **30**, 171–182 (2001).
11. J. H. Singer, L. Lassova, N. Vardi, J. S. Diamond, Coordinated multivesicular release at a mammalian ribbon synapse. *Nat. Neurosci.* **7**, 826–833 (2004).
12. C. W. Graydon, S. Cho, G. L. Li, B. Kachar, H. von Gersdorff, Sharp $Ca2^+$ nanodomains beneath the ribbon promote highly synchronous multivesicular release at hair cell synapses. *J. Neurosci.* **31**, 16637–16650 (2011).
13. J. E. Heuser, T. S. Reese, Evidence for recycling of synaptic vesicle membrane during transmitter release at the frog neuromuscular junction. *J. Cell Biol.* **57**, 315–344 (1973).
14. B. Ceccarelli, W. P. Hurlbut, A. Mauro, Depletion of vesicles from frog neuromuscular junctions by prolonged tetanic stimulation. *J. Cell Biol.* **54**, 30–38 (1972).
15. A. Albillos, G. Dernick, H. Horstmann, W. Almers, G. A. de Toledo, M. Lindau, The exocytotic event in chromaffin cells revealed by patch amperometry. *Nature* **389**, 509–512 (1997).
16. V. A. Klyachko, M. B. Jackson, Capacitance steps and fusion pores of small and large-dense-core vesicles in nerve terminals. *Nature* **418**, 89–92 (2002).
17. J. W. Taraska, D. Perrais, M. Ohara-Imaizumi, S. Nagamatsu, W. Almers, Secretory granules are recaptured largely intact after stimulated exocytosis in cultured endocrine cells. *Proc. Natl. Acad. Sci. U.S.A.* **100**, 2070–2075 (2003).
18. L. He, X. S. Wu, R. Mohan, L. G. Wu, Two modes of fusion pore opening revealed by cell-attached recordings at a synapse. *Nature* **444**, 102–105 (2006).
19. Q. Zhang, Y. Li, R. W. Tsien, The dynamic control of kiss-and-run and vesicular reuse probed with single nanoparticles. *Science* **323**, 1448–1453 (2009).
20. A. Anantharam, M. A. Bittner, R. L. Aikman, E. L. Stuenkel, S. L. Schmid, D. Axelrod, R. W. Holz, A new role for the dynamin GTPase in the regulation of fusion pore expansion. *Mol. Biol. Cell* **22**, 1907–1918 (2011).
21. H. C. Chiang, W. Shin, W. D. Zhao, E. Hamid, J. Sheng, M. Baydyuk, P. J. Wen, A. Jin, F. Momboisse, L. G. Wu, Post-fusion structural changes and their roles in exocytosis and endocytosis of dense-core vesicles. *Nat. Commun.* **5**, 3356 (2014).
22. W. D. Zhao, E. Hamid, W. Shin, P. J. Wen, E. S. Krystofiak, S. A. Villarreal, H. C. Chiang, B. Kachar, L. G. Wu, Hemi-fused structure mediates and controls fusion and fission in live cells. *Nature* **534**, 548–552 (2016).
23. W. Shin, L. Ge, G. Arpino, S. A. Villarreal, E. Hamid, H. Liu, W. D. Zhao, P. J. Wen, H. C. Chiang, L. G. Wu, Visualization of membrane pore in live cells reveals a dynamic-pore theory governing fusion and endocytosis. *Cell* **173**, 934–945.e12 (2018).
24. W. Shin, G. Arpino, S. Thiyagarajan, R. Su, L. Ge, Z. M. Dargh, X. Guo, L. Wei, O. Shupliakov, A. Jin, B. O'S, L.-G. Wu, Vesicle shrinking and enlargement play opposing roles in the release of exocytotic contents. *Cell Rep.* **30**, 421–431.e7 (2020).
25. W. Shin, L. Wei, G. Arpino, L. Ge, X. Guo, C. Y. Chan, E. Hamid, O. Shupliakov, C. K. E. Bleck, L.-G. Wu, Preformed Ω-profile closure and kiss-and-run mediate endocytosis and diverse endocytic modes in neuroendocrine chromaffin cells. *Neuron* **109**, 3119–3134.e5 (2021).
26. N. Hosoi, M. Holt, T. Sakaba, Calcium dependence of exo- and endocytotic coupling at a glutamatergic synapse. *Neuron* **63**, 216–229 (2009).
27. X. S. Wu, B. D. McNeil, J. Xu, J. Fan, L. Xue, E. Melicoff, R. Adachi, L. Bai, L. G. Wu, Ca(2+) and calmodulin initiate all forms of endocytosis during depolarization at a nerve terminal. *Nat. Neurosci.* **12**, 1003–1010 (2009).
28. P. J. Wen, S. Grenklo, G. Arpino, X. Tan, H. S. Liao, J. Heureaux, S. Y. Peng, H. C. Chiang, E. Hamid, W. D. Zhao, W. Shin, T. Näreoja, E. Evergren, Y. Jin, R. Karlsson, S. N. Ebert, A. Jin, A. P. Liu, O. Shupliakov, L. G. Wu, Actin dynamics provides membrane tension to merge fusing vesicles into the plasma membrane. *Nat. Commun.* **7**, 12604 (2016).
29. I. Hafez, A. Stolpe, M. Lindau, Compound exocytosis and cumulative fusion in eosinophils. *J. Biol. Chem.* **278**, 44921–44928 (2003).
30. T. Nemoto, R. Kimura, K. Ito, A. Tachikawa, Y. Miyashita, M. Iino, H. Kasai, Sequential-replenishment mechanism of exocytosis in pancreatic acini. *Nat. Cell Biol.* **3**, 253–258 (2001).
31. J. A. Pickett, J. M. Edwardson, Compound exocytosis: Mechanisms and functional significance. *Traffic* **7**, 109–116 (2006).
32. S. Rudolph, L. Overstreet-Wadiche, J. I. Wadiche, Desynchronization of multivesicular release enhances Purkinje cell output. *Neuron* **70**, 991–1004 (2011).
33. N. G. Gubernator, H. Zhang, R. G. W. Staal, E. V. Mosharov, D. B. Pereira, M. Yue, V. Balsanek, P. A. Vadola, B. Mukherjee, R. H. Edwards, D. Sulzer, D. Sames, Fluorescent false neurotransmitters visualize dopamine release from individual presynaptic terminals. *Science* **324**, 1441–1444 (2009).

34. P. Bhat, P. Thorn, Myosin 2 maintains an open exocytic fusion pore in secretory epithelial cells. *Mol. Biol. Cell* **20**, 1795–1803 (2009).
35. N. R. Gandasi, S. Barg, Contact-induced clustering of syntaxin and munc18 docks secretory granules at the exocytosis site. *Nat. Commun.* **5**, 3914 (2014).
36. M. B. Hoppa, E. Jones, J. Karanauskaite, R. Ramracheya, M. Braun, S. C. Collins, Q. Zhang, A. Clark, L. Eliasson, C. Genoud, P. E. MacDonald, A. G. Monteith, S. Barg, J. Galvanovskis, P. Rorsman, Multivesicular exocytosis in rat pancreatic beta cells. *Diabetologia* **55**, 1001–1012 (2012).
37. L. He, L. Xue, J. Xu, B. D. McNeil, L. Bai, E. Melicoff, R. Adachi, L. G. Wu, Compound vesicle fusion increases quantal size and potentiates synaptic transmission. *Nature* **459**, 93–97 (2009).
38. Q. Fang, K. Berberian, L. W. Gong, I. Hafez, J. B. Sørensen, M. Lindau, The role of the C terminus of the SNARE protein SNAP-25 in fusion pore opening and a model for fusion pore mechanics. *Proc. Natl. Acad. Sci. U.S.A.* **105**, 15388–15392 (2008).
39. A. T. Brunger, U. B. Choi, Y. Lai, J. Leitz, Q. Zhou, Molecular mechanisms of fast neurotransmitter release. *Annu. Rev. Biophys.* **47**, 469–497 (2018).
40. K. Berberian, A. J. Torres, Q. Fang, K. Kisler, M. Lindau, F-actin and myosin II accelerate catecholamine release from chromaffin granules. *J. Neurosci.* **29**, 863–870 (2009).
41. Q. Gan, S. Watanabe, Synaptic vesicle endocytosis in different model systems. *Front. Cell. Neurosci.* **12**, 171 (2018).
42. B. Ceccarelli, W. P. Hurlbut, A. Mauro, Turnover of transmitter and synaptic vesicles at the frog neuromuscular junction. *J. Cell Biol.* **57**, 499–524 (1973).
43. S. Watanabe, B. R. Rost, M. Camacho-Pérez, M. W. Davis, B. Söhl-Kielczynski, C. Rosenmund, E. M. Jorgensen, Ultrafast endocytosis at mouse hippocampal synapses. *Nature* **504**, 242–247 (2013).
44. C. M. Persoon, A. Moro, J. P. Nassal, M. Farina, J. H. Broeke, S. Arora, N. Dominguez, J. R. T. Weering, R. F. Toonen, M. Verhage, Pool size estimations for dense-core vesicles in mammalian CNS neurons. *EMBO J.* **37**, (2018).
45. A. Ichikawa, Fine structural changes in response to hormonal stimulation of the perfused canine pancreas. *J. Cell Biol.* **24**, 369–385 (1965).
46. G. T. Alvarez, J. M. Fernandez, Compound versus multigranular exocytosis in peritoneal mast cells. *J. Gen. Physiol.* **95**, 397–409 (1990).
47. S. Scepek, M. Lindau, Focal exocytosis by eosinophils--Compound exocytosis and cumulative fusion. *EMBO J.* **12**, 1811–1817 (1993).
48. G. Matthews, P. Sterling, Evidence that vesicles undergo compound fusion on the synaptic ribbon. *J. Neurosci.* **28**, 5403–5411 (2008).
49. N. C. Shaner, G. G. Lambert, A. Chammas, Y. Ni, P. J. Cranfill, M. A. Baird, B. R. Sell, J. R. Allen, R. N. Day, M. Israelsson, M. W. Davidson, J. Wang, A bright monomeric green fluorescent protein derived from Branchiostoma lanceolatum. *Nat. Methods* **10**, 407–409 (2013).
50. R. W. Holz, M. D. Hlubek, S. D. Sorensen, S. K. Fisher, T. Balla, S. Ozaki, G. D. Prestwich, E. L. Stuenkel, M. A. Bittner, A pleckstrin homology domain specific for phosphatidylinositol 4,5-bisphosphate (PtdIns-4,5-P2) and fused to green fluorescent protein identifies plasma membrane PtdIns-4,5-P2 as being important in exocytosis. *J. Biol. Chem.* **275**, 17878–17885 (2000).
51. G. Di Paolo, H. S. Moskowitz, K. Gipson, M. R. Wenk, S. Voronov, M. Obayashi, R. Flavell, R. M. Fitzsimonds, T. A. Ryan, P. De Camilli, Impaired PtdIns(4,5)P2 synthesis in nerve terminals produces defects in synaptic vesicle trafficking. *Nature* **431**, 415–422 (2004).
52. R. S. Gormal, T. H. Nguyen, S. Martin, A. Papadopulos, F. A. Meunier, An acto-myosin II constricting ring initiates the fission of activity-dependent bulk endosomes in neurosecretory cells. *J. Neurosci.* **35**, 1380–1389 (2015).
53. P. J. Wen, S. L. Osborne, M. Zanin, P. C. Low, H. T. A. Wang, S. M. Schoenwaelder, S. P. Jackson, R. Wedlich-Söldner, B. Vanhaesebroeck, D. J. Keating, F. A. Meunier, Phosphatidylinositol(4,5)bisphosphate coordinates actin-mediated mobilization and translocation of secretory vesicles to the plasma membrane of chromaffin cells. *Nat. Commun.* **2**, 491 (2011).
54. I. Milosevic, J. B. Sørensen, T. Lang, M. Krauss, G. Nagy, V. Haucke, R. Jahn, E. Neher, Plasmalemmal phosphatidylinositol-4,5-bisphosphate level regulates the releasable vesicle pool size in chromaffin cells. *J. Neurosci.* **25**, 2557–2565 (2005).
55. T. F. Martin, PI(4,5)P2-binding effector proteins for vesicle exocytosis. *Biochim. Biophys. Acta* **1851**, 785–793 (2015).
56. A. M. Walter, R. Müller, B. Tawfik, K. D. B. Wierda, P. S. Pinheiro, A. Nadler, A. W. McCarthy, I. Ziomkiewicz, M. Kruse, G. Reither, J. Rettig, M. Lehmann, V. Haucke, B. Hille, C. Schultz, J. B. Sørensen, Phosphatidylinositol 4,5-bisphosphate optical uncaging potentiates exocytosis. *eLife* **6**, e30203 (2017).
57. G. R. Hammond, Y. Sim, L. Lagnado, R. F. Irvine, Reversible binding and rapid diffusion of proteins in complex with inositol lipids serves to coordinate free movement with spatial information. *J. Cell Biol.* **184**, 297–308 (2009).
58. M. Lindau, E. Neher, Patch-clamp techniques for time-resolved capacitance measurements in single cells. *Pflug. Arch. Eur. J. Physiol.* **411**, 137–146 (1988).
59. D. Perrais, I. C. Kleppe, J. W. Taraska, W. Almers, Recapture after exocytosis causes differential retention of protein in granules of bovine chromaffin cells. *J. Physiol.* **560**, 413–428 (2004).
60. C. Smith, E. Neher, Multiple forms of endocytosis in bovine adrenal chromaffin cells. *J. Cell Biol.* **139**, 885–894 (1997).

Acknowledgments: We thank C. Smith for STED microscopy support. **Funding:** This work was supported by the National Institute of Neurological Disorders and Stroke Intramural Research Program (ZIA NS003009-16 and ZIA NS003105-11) to L.-G.W. **Author contributions:** L.G. did most of the FFN511-related STED imaging. W.S. did most of the PH_G/A532-related STED imaging. G.A. performed electron microscopy. C.K.E.B. assisted in the electron microscopic work. C.Y.C., L.W., and W.Z. performed confocal imaging. L.G. wrote the experimental results. L.-G.W. supervised the project and wrote the manuscript with help from all the other authors. **Competing interests:** The authors declare that they have no competing interests. **Data and materials availability:** All data needed to evaluate the conclusions in the paper are present in the paper and/or the Supplementary Materials.

Submitted 28 September 2021
Accepted 3 May 2022
Published 17 June 2022
10.1126/sciadv.abm6049